Materials Research Bulletin 205 (2027) 114357

Contents lists available at ScienceDirect

Materials Research Bulletin

journal homepage: www.elsevier.com/locate/matresbu

Research Papers

Accurate calculation of anisotropic compressibility and pressure-induced phase transition in organic–inorganic hybrid semiconductor β-ZnTe(en)$_{0.5}$

Xuwei Gong [a,b,1], Biao Zeng [a,b,1], Yong Zhang [c], Yi-Yang Sun [a,b,*]

[a] State Key Laboratory of High-Performance Ceramics, Shanghai Institute of Ceramics, Chinese Academy of Sciences, Shanghai 201899, China
[b] Center of Materials Science and Optoelectronics Engineering, University of Chinese Academy of Sciences, Beijing 100049, China
[c] Department of Electrical and Computer Engineering, University of North Carolina at Charlotte, Charlotte, NC 28223, USA

ARTICLE INFO

Keywords:
Organic–inorganic hybird
High pressure
Density functional
Compressibility
Luminescence

ABSTRACT

The hybrid semiconductor β-ZnTe(en)$_{0.5}$ (en = $C_2N_2H_8$, ethylenediamine) serves as a prototypical organic–inorganic optoelectronic material characterized by a superlattice structure with strongly anisotropic properties. To accurately describe its elastic stiffness tensors, axial compressibilities, and Poisson's ratios, we evaluated various exchange–correlation functionals. Our results demonstrate that only the dispersion-corrected PBE functionals, particularly PBE-D3(BJ), accurately reproduce the strongly anisotropic mechanical response. Using this method, we investigated the structural evolution of this material under hydrostatic pressure. We identified a structural phase transition at 2.4 GPa, which lies within the experimentally observed transition range of 2.1–2.9 GPa, and determined that the high-pressure structure adopts $P2_1/n$ space group symmetry. Furthermore, we simulated the Raman and infrared spectra to provide theoretical insights and assist in further experimental characterization of the low- and high-pressure phases. This work provides unique insights into selecting appropriate functionals to simulate complex organic–inorganic hybrid structures.

1. Introduction

Organic–inorganic hybrid semiconductors combine the rigidity of the inorganic framework with the flexibility of the organic components [1–5]. Although halide hybrid perovskites, e.g., methylammonium lead iodide ($CH_3NH_3PbI_3$) and its derivatives, have been extensively investigated in fields such as photovoltaics and light-emitting diodes, their practical applications are hindered by environmental instability [6–12]. There is a practical need to explore novel hybrid semiconductors that exhibit both exceptional stability and excellent optoelectronic properties. In this context, β-ZnTe(en)$_{0.5}$ (en = $C_2N_2H_8$, ethylenediamine) was first reported in 2000 and has stood out as a member of a large family of II–VI-based hybrid structures owing to its outstanding properties [13–17]. Unlike conventional inorganic superlattices and most other hybrid materials, β-ZnTe(en)$_{0.5}$ features both long- and short-range order, yielding crystallinity that rivals that of high-quality elemental and binary semiconductors and is the highest among man-made superlattices [18]. Benefiting from a thermal degradation activation energy exceeding 1.6 eV, it demonstrates excellent room-temperature stability and is currently the longest-lived hybrid semiconductor known [18,19]. Furthermore, it exhibits pronounced excitonic effects, resembling those of a 2D semiconductor [20], and is one of the few non-oxide semiconductors that display zero or even negative thermal expansion [21]. Coupled with a high valence band maximum and a wide band gap of over 3.5 eV, it also shows potential to be doped as a p-type transparent conductor [22].

As a biaxial crystal composed of alternating two-monolayer ZnTe sheets and en spacers, β-ZnTe(en)$_{0.5}$ exhibits strong anisotropy in its physical properties, as previously shown in its electronic and optical properties and thermal expansion [21,22]. Recently, a hydrostatic-pressure study of this material [23] has revealed its highly anisotropic elastic response, including a particularly high interlayer compressibility and low-threshold pressure-induced phase transitions at 2.1 and 3.3 GPa, suggesting potential sensing and memory applications. Similar pressure-induced phenomena have been extensively reported in metal organic frameworks (MOFs) and covalent organic frameworks (COFs), where external pressure can induce pronounced anisotropic compressibility, breathing behavior, and structural phase transitions [24–27]. The study on β-ZnTe(en)$_{0.5}$ raises two interesting computational issues that need to be addressed. First, the axial compression behavior deviates drastically from what was predicted by previous density functional theory (DFT) calculations and molecular dynamics

* Corresponding author at: State Key Laboratory of High-Performance Ceramics, Shanghai Institute of Ceramics, Chinese Academy of Sciences, Shanghai 201899, China.
E-mail addresses: yong.zhang@uncc.edu (Y. Zhang), yysun@mail.sic.ac.cn (Y.-Y. Sun).
[1] These authors contributed equally to this work.

https://doi.org/10.1016/j.materresbull.2026.114357
Received 2 June 2026; Received in revised form 29 July 2026; Accepted 29 July 2026
Available online 3 August 2026

Table 1
Calculated elastic constants C_{ij} (in GPa) of β-ZnTe(en)$_{0.5}$ using different exchange–correlation functionals, in comparison with previously reported theoretical values [28].

Functionals	C_{11}	C_{12}	C_{13}	C_{22}	C_{23}	C_{33}	C_{44}	C_{55}	C_{66}
PBE	34.7	15.4	7.3	30.5	16.6	49.7	16.6	3.9	7.8
PBEsol	36.5	20.4	10.4	38.3	22.0	56.4	19.9	4.1	8.4
SCAN	46.4	17.3	5.9	34.0	18.8	59.0	19.7	7.4	11.5
r^{2}SCAN	45.4	18.9	8.3	36.3	20.3	55.7	12.7	4.1	8.9
SCAN+rVV10	53.9	22.0	6.6	42.2	24.3	58.1	24.1	2.3	9.8
DFT-PBE [28]	43.1	14.1	7.4	32.5	18.0	51.6	18.0	5.8	8.2
MD [28]	41.9	14.9	8.8	39.1	18.9	55.3	21.5	1.4	7.7
PBE-D3	30.9	19.0	9.3	39.9	23.8	57.0	20.6	3.7	9.3
PBE-D3 (BJ)	31.2	19.5	9.5	40.8	24.2	56.9	20.9	3.6	9.2

(MD) simulations [28]. Second, structural information regarding the high-pressure phases, such as their exact space groups, remains unknown, although it has been speculated that the phase transitions are dominated by conformational changes of the en molecule.

The reliability of exchange–correlation functionals is commonly judged by their ability to accurately describe basic material properties, such as lattice constants, electronic band structures, and phonon frequencies, which are often the first quantities to be measured. Elastic properties are rarely included in such benchmarks because they are not readily available for new materials. A recent study compared the accuracy of different functionals for calculating the elastic constants and pressure-induced phase transitions of group IV semiconductors [29]. β-ZnTe(en)$_{0.5}$ is a unique and clean prototype structure, structurally much more complex than elemental semiconductors, for accurately assessing computational approaches to different material properties, including, in this case, the elastic properties and phase transitions of a hybrid structure for which dispersion corrections are expected to be significant.

In this study, DFT calculations were conducted to explore the pressure-induced phase transition of β-ZnTe(en)$_{0.5}$ and to address the issue of accurately predicting the mechanical anisotropy of this material. We systematically evaluated several exchange–correlation functionals by comparing their predictions of elastic stiffness tensors, axial compressibilities, and Poisson's ratios. Our results show that the dispersion-corrected PBE-D3(BJ) functional accurately reproduces the strongly anisotropic mechanical response, thereby resolving the discrepancy between previous theoretical results and experimental findings. Furthermore, our study elucidates the structural evolution under high pressure and identifies the role of the flexible organic layers during the phase transition. The predicted high-pressure structure is further corroborated by comparing the calculated transition pressure with the experimental result. We also simulated Raman and infrared spectra for both the low-pressure and high-pressure phases. This work provides unique insights into selecting appropriate functionals to simulate complex organic–inorganic hybrid structures.

2. Computational methods

All DFT calculations in this work were performed using the Vienna Ab initio Simulation Package (VASP) [30]. The interactions between ionic cores and valence electrons were described using the projector-augmented-wave (PAW) method [31,32], and the electronic wave functions were expanded in a plane-wave basis set. To obtain accurate lattice constants and axial compressibilities, we compared several exchange–correlation functionals, including the Perdew–Burke–Ernzerhof (PBE) [33], PBEsol [34], PBE-D3 [35], and PBE-D3(BJ) [35,36]. At the meta-GGA level, we adopted the strongly constrained and appropriately normed (SCAN) functional [37], its regularized-restored version (r^{2}SCAN) [38], and the SCAN+rVV10 functional [39], which incorporates the revised Vydrov–Van Voorhis nonlocal van der Waals (vdW) correlation functional [40–43].

To ensure the accuracy of the calculated results, strict convergence criteria were applied. The plane-wave cutoff energy was set to 1200 eV.

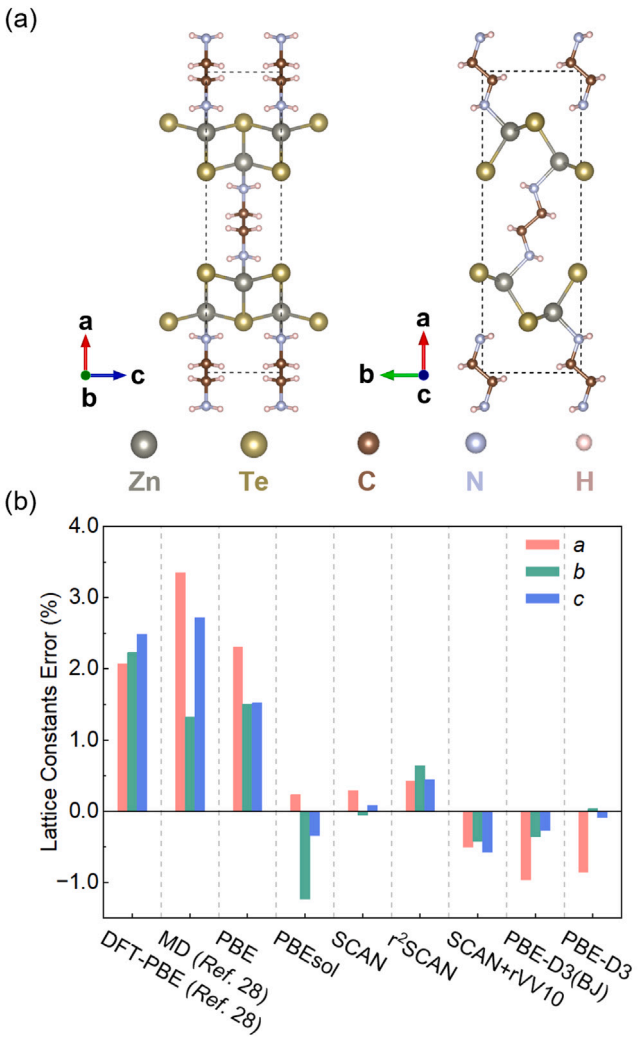

Fig. 1. (a) Crystal structure of β-ZnTe(en)$_{0.5}$ viewed along two directions. (b) Relative errors of the calculated lattice constants with respect to the experimental values [21]. The results obtained using different functionals in this work are compared with previously reported theoretical values [28].

The Brillouin zone was sampled using a 2 × 8 × 10 k-point mesh. The energy and force convergence criteria were set to 10^{-8} eV and 0.001 eV/Å, respectively. To evaluate the macroscopic mechanical response and vibrational spectroscopic properties of β-ZnTe(en)$_{0.5}$, the elastic constants C_{ij} and the Γ-point phonon modes were calculated using the finite-difference method [44–48], whereas the dielectric tensors

and the Born effective charge tensors were obtained using density-functional perturbation theory [49–51]. The Raman tensor $R_{ij}^{(\nu)}$ was calculated from the partial derivative of the macroscopic dielectric tensor ε_{ij} with respect to the normal coordinate Q_ν of the νth phonon mode [52–54], according to

$$R_{ij}^{(\nu)} = \frac{\partial \varepsilon_{ij}}{\partial Q_\nu}. \tag{1}$$

For the orientation-averaged Raman response, the Raman activity of each mode was evaluated from the rotational invariants of the Raman tensor [54],

$$A_\nu = 45\bar{\alpha}_\nu^2 + 7\beta_\nu^2, \tag{2}$$

where $\bar{\alpha}_\nu$ and β_ν^2 are the isotropic and anisotropic invariants of $R^{(\nu)}$, respectively. For the polarization-averaged infrared response, the intensity of the νth phonon mode was determined by the mode-induced change in the macroscopic polarization [55], which can be written as

$$\Delta\mathbf{P}^{(\nu)} = \frac{1}{\Omega}\sum_s \mathbf{Z}_s^* \cdot \Delta\boldsymbol{\tau}_s^{(\nu)}, \tag{3}$$

where $\Delta\mathbf{P}^{(\nu)}$ is the change in macroscopic polarization induced by the νth phonon mode, Ω is the unit-cell volume, $\mathbf{Z}_s^*$ is the Born effective charge tensor of atom s, and $\Delta\boldsymbol{\tau}_s^{(\nu)}$ is the displacement vector of atom s associated with the νth phonon mode.

3. Results and discussion

3.1. Lattice constants of β-ZnTe(en)$_{0.5}$

As illustrated in Fig. 1(a), β-ZnTe(en)$_{0.5}$ belongs to the *Pnnm* space group, featuring a layered structure stacked along the *a*-axis and an extended intralayer network throughout the *bc* plane. The inorganic layers consist of two-monolayer-thick ZnTe (110) slabs and are connected by en molecules via covalent bonding between Zn and N atoms [18]. At 4.2 K, the experimental lattice constants of β-ZnTe(en)$_{0.5}$ are a = 17.1983 Å, b = 5.6569 Å, and c = 4.3429 Å [21], where the *a*- and *b*-axes are interchanged compared to previous work [23]. We first evaluated the effects of different exchange–correlation functionals on the lattice constants *a*, *b*, and *c*. As shown in Fig. 1(b), all of these functionals yield lattice constants with generally acceptable accuracy, although some functionals perform slightly better than others. We show below that although some functionals perform nearly as well in predicting the lattice constants, i.e., in locating the equilibrium structure at the energy minimum, they may behave rather differently in describing the energy landscape away from the minimum, such as in the calculation of axial compressibility.

3.2. Elastic constants and axial compressibilities of β-ZnTe(en)$_{0.5}$

The axial compressibility κ_i can be obtained either from the pressure dependence of the lattice constants or from the elastic stiffness tensor **C**. A recent experimental study reported κ_a = 2.26% GPa^{-1} and κ_b = 0.55% GPa^{-1} for the low-pressure phase, indicating that the interlayer direction is 4.11 times more compressible than the intralayer direction [23]. However, the values derived from the previously reported DFT-PBE (MD) results are κ_a = 1.54 (1.66)% GPa^{-1} and κ_b = 1.81 (1.41)% GPa^{-1}, yielding κ_a/κ_b = 0.85 (1.18) [28], which strongly deviates from the experimental findings. Intuitively, the crystal structure shown in Fig. 1(a) suggests that the *a*-axis should be the least stiff, because the molecule is expected to be highly compressible, whereas the *b*- and *c*-axes should be stiffer since both involve the inorganic sheets.

For small lattice deformations, each elastic constant C_{ij} is defined as the second derivative of the total energy E with respect to strain:

$$C_{ij} = \frac{1}{V_0}\frac{\partial^2 E}{\partial e_i \partial e_j}, \tag{4}$$

where V_0 is the equilibrium volume of the unit cell, and e_i and e_j are strain components expressed in Voigt notation [56]. To accurately evaluate the elastic properties, the calculated C_{ij} values are summarized in Table 1 for different functionals. The axial compressibility can then be calculated from the stress–strain relation [23]:

$$\mathbf{C}\boldsymbol{\varepsilon} = \boldsymbol{\sigma}. \tag{5}$$

Here, **C** is the elastic stiffness tensor, $\boldsymbol{\varepsilon}$ is the strain vector, and $\boldsymbol{\sigma}$ is the stress vector. For hydrostatic pressure, the stress vector is taken to be $\boldsymbol{\sigma} = (-P, -P, -P, 0, 0, 0)^T$. Consequently, the axial compressibility can be expressed as the negative of the induced axial strain per unit hydrostatic pressure, i.e., $\kappa_i = -\varepsilon_i/P$. A detailed derivation is provided in the Supplementary Materials.

Fig. 2(a) shows the calculated axial compressibilities along the *a*-, *b*-, and *c*-axes. The experimental value for the *c*-axis is not yet available [23]. The calculated axial compressibilities along the *a*- and *b*-axes are sensitive to the choice of exchange–correlation functional. Fig. 2(b) presents the ratios $R_{a/b} = \kappa_a/\kappa_b$ and $R_{a/c} = \kappa_a/\kappa_c$. Except for PBE-D3 and PBE-D3(BJ), the results from all other functionals, including the vdW-corrected SCAN+rVV10, significantly deviate from the experimental values, with κ_a and κ_b being too close to each other. In particular, SCAN, r^{2}SCAN and the previous PBE calculation even yield $\kappa_a < \kappa_b$. These results overestimate the resistance to compression along the interlayer *a* direction while underestimating that along the intralayer *b* direction. Both the dispersion-corrected PBE-D3 and PBE-D3(BJ) functionals show good agreement with the experimental κ_a and κ_b values, yielding 2.50 (2.49)% GPa^{-1} and 0.68 (0.62)% GPa^{-1} for the *a*- and *b*-axes, respectively. The corresponding predicted κ_c values are 1.06 (1.08)% GPa^{-1}. These results confirm the highly compressible layer stacking axis of β-ZnTe(en)$_{0.5}$. This resolves the contradiction between the previous PBE- and MD-based predictions and the experimental results. Furthermore, the PBE-D3(BJ) functional yields superior quantitative accuracy, with an axial compressibility ratio $R_{a/b}$ in closest agreement with experiment. This demonstrates its capability to accurately predict the anisotropic mechanical response of the material. Note that, as seen in Table 1, for most functionals, the C_{11} values are either larger than or comparable to the C_{22} values. Only PBE-D3 and PBE-D3(BJ) yield a C_{11} value nearly half that of bulk zinc-blende ZnTe, whereas C_{33} remains close to the bulk value of 61.5 GPa [28]. This is understandable because the en molecules are aligned parallel to the *a*-axis, whereas the inorganic slabs perpendicular to the *a*-axis is more rigid.

We further evaluated the Poisson's ratios, whose detailed derivation is provided in the Supplementary Materials. In the *ab* and *bc* planes, the material displays conventional positive Poisson's ratios, with ν_{ab} = 0.5067, ν_{ba} = 0.5220, ν_{bc} = 0.3381, and ν_{cb} = 0.6383, which are all larger than the previously predicted values derived from the PBE results for C_{ij} [16]. It is noteworthy that ν_{ca} and ν_{ac} exhibit negative Poisson's ratios of −0.0944 and −0.0486, respectively, with magnitudes much larger than the previously reported values of ν_{ca} = −0.0111 and ν_{ac} = −0.0098. We examined the structure under compression along the *a* axis. The negative Poisson's ratio is connected to bond angles within the Zn-centered tetrahedrons. For clarity, we name the Te atom in the mirror plane of the *Pnnm* group as Te$_{in}$, while the other two Te atoms bonded to the Zn atoms as Te$_{out}$, which are out of the mirror plane. Reducing the lattice constant *a* by 1% will reduce the N–Zn–Te$_{in}$ angle from 104.07° to 103.25°, and meanwhile reduce the Te$_{out}$–Zn–Te$_{out}$ angle from 109.64° to 109.42°. Essentially, when the molecule is compressed along the *a* axis, the Zn atom is pushed down into the ZnTe sheet, which leads to the reduction of the *c* lattice constants, as can be visualized using Fig. 1(a). The same trend of these two bond angles is consistent with the negative Poisson's ratio obtained above. Given the best performance of the PBE-D3(BJ) functional in describing the mechanical properties of the system, the subsequent structural predictions of high-pressure phases and vibrational property simulations will be conducted using this functional.

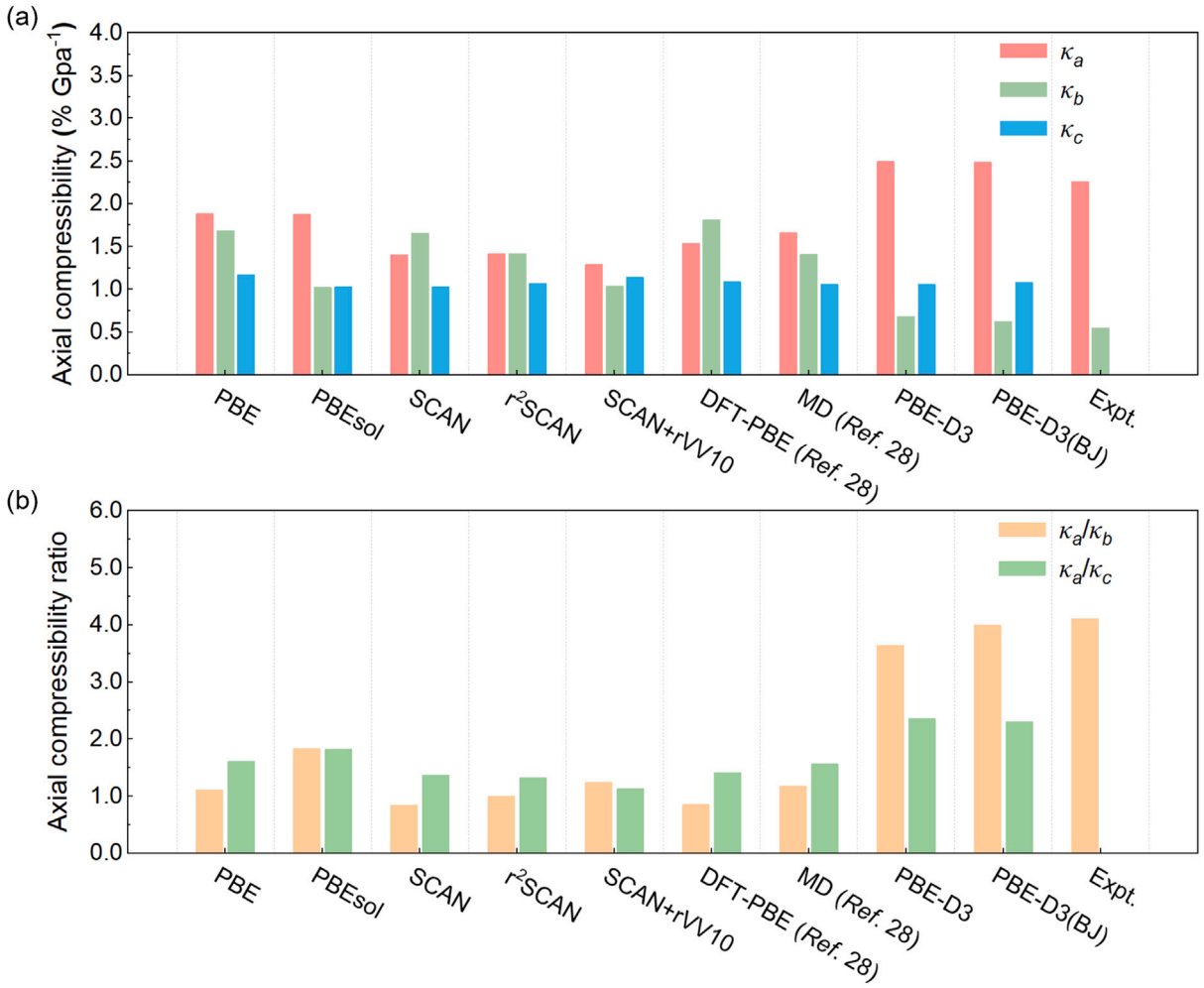

Fig. 2. (a) Axial compressibilities κ_i $(i = a, b, c)$ along the a-, b- and c-axes calculated using different exchange–correlation functionals, together with literature and experimental data [23,28]. (b) Axial compressibility ratios $R_{a/b} = \kappa_a/\kappa_b$ and $R_{a/c} = \kappa_a/\kappa_c$. Experimental values involving κ_c are not shown because κ_c has not been experimentally reported.

3.3. Phase transition of β-ZnTe(en)$_{0.5}$

Previous experimental studies have shown that β-ZnTe(en)$_{0.5}$ undergoes two reversible pressure-induced phase transitions at 2.1 GPa and 3.3 GPa. However, the detailed structural information of the high-pressure phases remains unclear [23]. Given the challenges of experimental determination of the detailed crystal structure of such a hybrid material under high pressure, it is necessary to predict the possible high-pressure structure through theoretical calculations and to explore the underlying phase transition mechanisms. Note that the experiments typically employed pressure-transmitting media (PTM), while our calculations just assume ideal hydrostatic loading of the bulk crystal without explicitly including the PTM. Unlike porous frameworks such as MOFs, where the medium can enter the pores and modify the mechanical response [24], β-ZnTe(en)$_{0.5}$ is a dense, non-porous superlattice. Therefore, such PTM-related effects are therefore expected to be negligible at least to the first phase transition pressure, which is supported by the fact that our calculated compression coefficients and first phase change pressure are in good agreement with the experimental results.

To search for possible high-pressure structures, random atomic displacements were introduced into the *Pnnm* structure to reduce its symmetry to *P*1. These low-symmetry structures are referred to as quasi-low-pressure structures because they remain structurally close to the parent *Pnnm* phase before the phase transition. A series of compressed structures was then generated by reducing the lattice constants according to the calculated axial compressibilities. After structural relaxation, we obtained the total energy versus volume (E–V) curve. As shown in Fig. 3, the E–V curve exhibits discontinuous changes at certain volumes. At each discontinuity point, both the cell shape and internal atomic positions change significantly compared with those at the preceding volume point, indicating a structural transition along the relaxation path. Similarly, the resulting structures are referred to as quasi-high-pressure structures because their space group symmetries have not yet been determined. Fig. 3 shows that the E–V curve does not exhibit an ideal single-step transition from the quasi-low-pressure branch to the quasi-high-pressure branch. Instead, several isolated points deviate from the main branch and fall on the extension of the neighboring branch. In addition, the first discontinuity, marked by the red box in Fig. 3, appears at a pressure of 4.6 GPa, which is higher than the experimentally observed phase-transition onset of 2.1 GPa. The more accurate phase transition pressure will be calculated below. Before that, we need to determine the symmetry of the high-pressure phase.

The low-pressure phase belongs to the orthorhombic *Pnnm* space group (No. 58), where the non-hydrogen atoms are distributed on the high-symmetry mirror planes at $z = 0$ and $z = 0.5$, with the en molecules exhibiting a TTT conformation [57]. As depicted in Fig. 4, to overcome the increasing interlayer steric hindrance under compression,

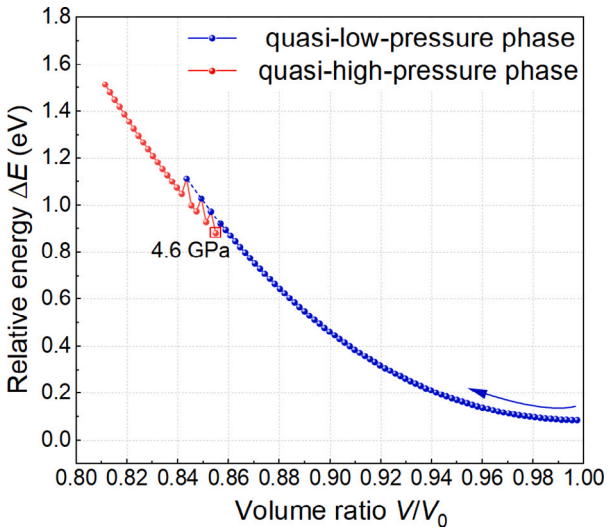

Fig. 3. Energy–volume (E–V) curve obtained from the relaxation of symmetry-broken quasi-low-pressure structures generated from the *Pnnm* phase. The energy and volume are referenced to the equilibrium energy E_0 and equilibrium volume V_0 of the low-pressure *Pnnm* phase, respectively; thus, the vertical axis represents $E-E_0$ and the horizontal axis represents V/V_0. The discontinuous energy changes indicate that structural transitions occur during the relaxation process. The arrow indicates that the volume decreases from right to left. The red box marks the first discontinuity, which corresponds to a pressure of 4.6 GPa. (For interpretation of the references to color in this figure legend, the reader is referred to the web version of this article.)

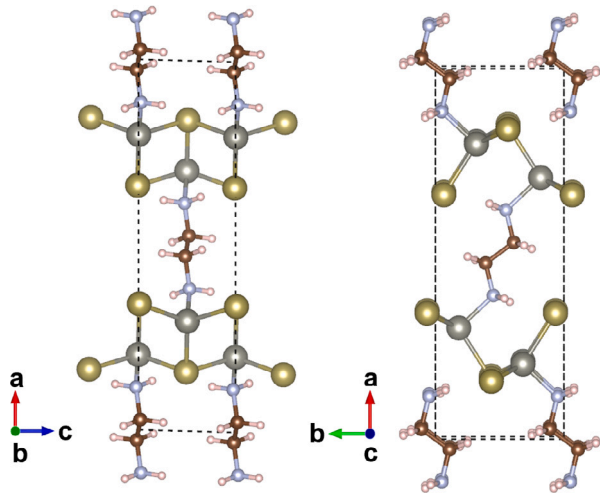

Fig. 4. Two views of the predicted $P2_1/n$ phase of β-ZnTe(en)$_{0.5}$, showing the tilting of the en molecules and the preserved connectivity of the inorganic [ZnTe] framework.

the en molecules undergo tilting. This structural change forces the en molecules to deviate from the original mirror planes, thereby reducing the number of symmetry operations from 8 to 4. The overall structure transforms into a monoclinic phase with the $P2_1/n$ space group (No. 14). In contrast, the response of the inorganic [ZnTe] framework under high pressure manifests itself as adaptive volume compression and local fine-tuning to match the lower symmetry, while its long-range topological connectivity is preserved.

We employed the Birch–Murnaghan equation of state to fit the calculated E–V data points for the two phases [29]. According to the relation $P = -\mathrm{d}E/\mathrm{d}V$, the phase transition pressure is equal to the negative slope of the common tangent of the E–V curves of the two phases.

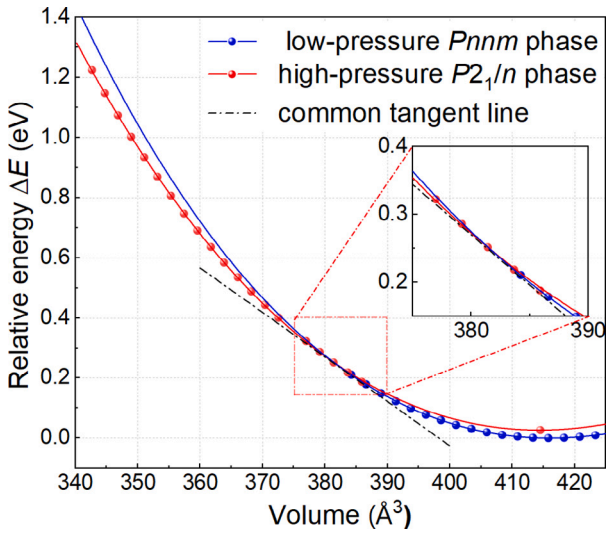

Fig. 5. Energy–volume (E–V) curves for the low-pressure *Pnnm* phase and the high-pressure $P2_1/n$ phase. The energy is referenced to the minimum of the low-pressure E–V curve. The solid curves are Birch–Murnaghan equation of state fits to the calculated data points. The dash-dotted line represents the common tangent of the two E–V curves, whose negative slope gives the transition pressure P_t. The inset shows a magnified view of the region around the tangent points.

As shown in Fig. 5, by solving for this common tangent, the theoretical transition pressure was determined to be 2.4 GPa, which lies within the experimentally observed transition interval of 2.1–2.9 GPa. This agreement suggests that the predicted monoclinic phase corresponds to the experimentally observed second phase. The optimized structure corresponding to 2.4 GPa shows that the en molecules tilt while retaining their overall TTT conformation, with the N1–C1–C2–N2 dihedral angle kept at 180°. However, the Zn–N1–C1–C2 and Zn–N2–C2–C1 dihedral angles change slightly from 180° to 178.3°. Furthermore, since the accompanying unit-cell shear deformation only causes the β angle to deviate marginally from 90° to 91.4°, this monoclinic structure can be described as pseudo-orthorhombic [58]. The detailed crystallographic parameters of this high-pressure phase are provided in CIF format in the Supplementary Materials.

To assess the robustness of this local search, we generated a set of initial structures by applying random perturbations of up to 5% to the atomic coordinates and relaxed each structure independently under compression (see the Supplementary Materials). We found that the volume at which the structural discontinuity appears varies with the initial perturbation, reflecting the path-dependent nature of the local relaxation. Nevertheless, symmetry analysis of the obtained structures consistently identifies them as the same $P2_1/n$ phase, confirming that the predicted $P2_1/n$ phase does not depend on the initial distorted configuration.

3.4. Discussion on the phase transitions

The approach above for determining the atomic structure after phase transition is applicable to the case where the phase transition involves only simple and local distortions to the original structure. It will fail if the rearrangement of the bonding network is extensive. By examining the experimental XRD results [23], the peaks after phase transitions mainly involve peak splitting rather than extensive new peaks, suggesting that the distortions are mainly local and the approach employed above is acceptable.

Regarding the new $P2_1/n$ phase, the predicted phase transition pressure is in good agreement with experimental measurement. Moreover, during the study on Raman and infrared spectra below, there

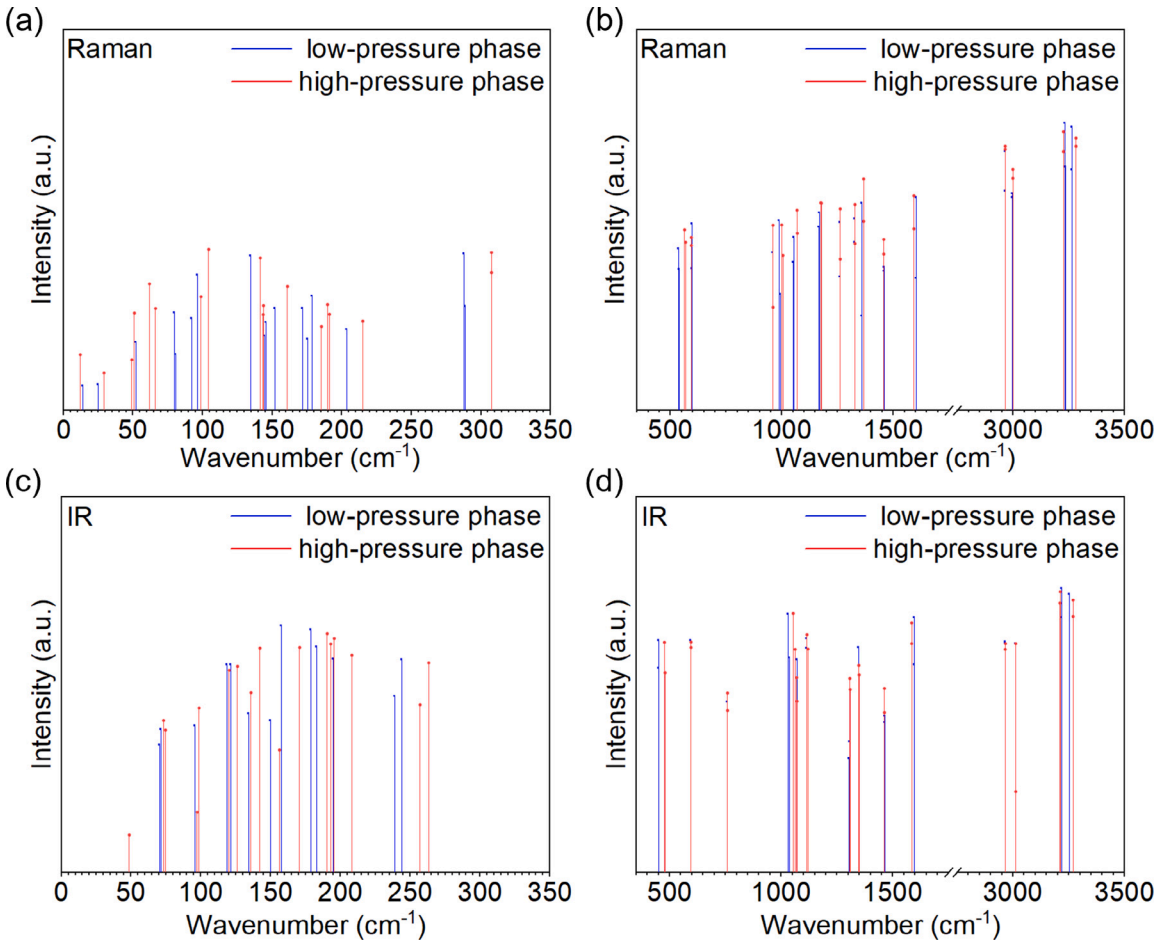

Fig. 6. Theoretically calculated vibrational spectra of the low-pressure and high-pressure phases of β-ZnTe(en)$_{0.5}$. Raman spectra in the ranges of (a) 0–350 cm^{-1} and (b) 350–3500 cm^{-1}. IR spectra in the ranges of (c) 0–350 cm^{-1} and (d) 350–3500 cm^{-1}. The intensities are plotted on a logarithmic scale to enhance the visibility of weak peaks.

are not any imaginary modes found in our calculations, suggesting that the $P2_1/n$ phase is indeed a metastable phase. Thus, we have reasonable confidence that the identified structure is true. Regarding the further phase transition to the third phase at higher pressure, we fail to determine its atomic structure. To improve the approach, one may consider more global algorithms such as USPEX [59] and CALYPSO [60] to search for new structures. However, the 32-atom unit cell of β-ZnTe(en)$_{0.5}$ renders these approaches too complicated to locate the global minimum of the configuration space. Another possibility is the reconstruction into larger unit cells, even though this lacks experimental evidence so far as the XRD results do not show new peaks corresponding to doubling of lattice constants along a and b directions. The determination of the third phase may need future experiments to provide more insights.

Another limitation on the approach employed above is the temperature effect. Ideally, one needs to calculate the Gibbs free energy to determine the accurate phase transition pressure. Instead, we calculated the total energies at 0 K and ignored the effect of phonons which contributes to the entropy and the temperature-dependence of enthalpy. Therefore, the calculated phase transition pressure of 2.4 GPa should be considered as an approximation.

3.5. Raman and infrared spectroscopic analysis of β-ZnTe(en)$_{0.5}$

To assist the experimental characterization of the low-pressure and high-pressure phases of β-ZnTe(en)$_{0.5}$, we further calculated Raman and infrared (IR) spectra. Fig. 6(a) and (b) present the calculated Raman spectra in the low- and high-frequency regions, respectively, for the low-pressure phase at $P = 0$ GPa and the high-pressure phase at $P = 2.4$ GPa. The calculated Raman spectrum of the low-pressure $Pnnm$ phase reproduces the main features reported in previous literature [18]. Although the total number of Raman-active modes remains unchanged after the phase transition, the symmetry lowering from the $Pnnm$ phase to the $P2_1/n$ phase modifies the Raman symmetry classification. Specifically, the four Raman-active species in the orthorhombic phase, A_g, $B_{1\ g}$, $B_{2\ g}$, and $B_{3\ g}$, are regroup into only two monoclinic species, A_g and B_g. In the low-frequency region, most Raman modes associated with the inorganic [ZnTe] framework exhibit a shift toward higher frequencies, i.e., a blue shift, after the phase transition. In the high-frequency region, the Raman features can be mostly attributed to the stretching vibrations of the en molecules. These modes remain within a similar frequency range across the phase transition, suggesting that the intramolecular bonding framework is largely retained under pressure. Meanwhile, the changes in peak position and intensity indicate that the local environment of the en molecules is modified in the high-pressure phase. Detailed assignments of the Raman-active modes in both the low-pressure and high-pressure phases are given in the Supplementary Materials.

Fig. 6(c) and (d) present the calculated IR spectra of the low-pressure and high-pressure phases. Changes in the IR spectra are observed across the phase transition because the structural transformation modifies the symmetry classification of the IR-active modes from B_{1u}, B_{2u}, and B_{3u} to A_u and B_u. Detailed assignments of the IR-active modes in both the low-pressure and high-pressure phases are given in the Supplementary Materials.

4. Conclusion

In summary, this study investigated the high-pressure mechanical response and phase transition of β-ZnTe(en)$_{0.5}$ using density functional theory. By systematically comparing different exchange–correlation functionals, we show that the PBE-D3(BJ) functional can most accurately describe the elastic constants of this system, thereby resolving the discrepancy between earlier theoretical predictions and experimental measurements of its axial compressibility. Based on the resulting elastic constants, we further obtain Poisson's ratios that are more reliable than previous PBE-based estimates. In addition, our calculations predict the previously unreported c-axis compressibility. These results reflect the anisotropic mechanical response of this hybrid semiconductor. Under hydrostatic pressure, we predict that the tilting of the en molecules drives a symmetry reduction from the initial orthorhombic $Pnnm$ phase to a monoclinic $P2_1/n$ high-pressure phase, whose detailed crystal structure has not yet been experimentally determined. The calculated transition pressure of 2.4 GPa lies within the experimentally observed transition range, supporting the assignment of this predicted structure to the experimentally observed second phase and verifying the key role of the organic layers in the pressure response. We further predict the Raman and infrared spectra of both the low-pressure and high-pressure phases, providing theoretical references for future experimental characterization. Overall, this work highlights the importance of adopting an appropriate dispersion-corrected functional for complex organic–inorganic hybrid structures, where lattice constants alone are insufficient to assess the reliability of a functional and where mechanical response and pressure-induced phase transitions can be highly sensitive to the treatment of dispersion interactions.

CRediT authorship contribution statement

Xuwei Gong: Writing – original draft, Visualization, Formal analysis, Data curation. **Biao Zeng:** Formal analysis, Data curation, Conceptualization. **Yong Zhang:** Writing – review & editing, Formal analysis, Conceptualization. **Yi-Yang Sun:** Writing – review & editing, Supervision, Project administration, Formal analysis, Conceptualization.

Declaration of competing interest

The authors declare that they have no known competing financial interests or personal relationships that could have appeared to influence the work reported in this paper.

Acknowledgments

The work at UNC Charlotte was supported by ARO/Physical Properties of Materials (Grant No. W911NF-18-1-0079) and Bissell Distinguished Professorship.

Appendix A. Supplementary data

See the supplementary material for the derivations of the axial compressibilities and Poisson's ratios, the test of the structure search under different random perturbations, the structural information of the high-pressure phase, and the complete list of Raman- and infrared-active phonon modes for both phases.

Supplementary material related to this article can be found online at https://doi.org/10.1016/j.materresbull.2026.114357.

Data availability

Data will be made available on request.

References

[1] W. Liu, Y. Fang, J. Li, Copper iodide based hybrid phosphors for energy-efficient general lighting technologies, Adv. Funct. Mater. 28 (2018) 1705593.
[2] C. Sanchez, B. Julián, P. Belleville, M. Popall, Applications of hybrid organic–inorganic nanocomposites, J. Mater. Chem. 15 (2005) 3559.
[3] S. Morab, M.M. Sundaram, A. Pivrikas, Review on charge carrier transport in inorganic and organic semiconductors, Coatings 13 (2023) 1657.
[4] G. Kickelbick (Ed.), Hybrid Materials: Synthesis, Characterization, and Applications, Wiley - VCH, Weinheim, 2007.
[5] K. Luberda-Durnaś, P. Sanz-Camacho, A. González-Guillén, D. Mucha, E. Bielańska, W. Łasocha, Characterisation of organic–inorganic hybrid materials of the types $Zn_xCd_{1-x}Se$(1,3-diaminopropane)$_{1/2}$ and ZnS_ySe_{1-y}(1,3-diaminopropane)$_{1/2}$, Mater. Res. Bull. 100 (2018) 18–25.
[6] X. Shen, X. Lin, H. Su, Z. Zhang, T. Wu, J. Zhang, Y. Peng, Y. Zhang, S. Zhang, Z. Zhou, X. Meng, P. Gao, W. Chen, Y. Wu, C. Qin, Q. Han, Y. Wang, L. Han, Key advancements and emerging trends of perovskite solar cells in 2024–2025, Nano-Micro Lett. 18 (2026) 209.
[7] Z. Wei, Y. Zhao, J. Jiang, W. Yan, Y. Feng, J. Ma, Research progress on hybrid organic–inorganic perovskites for photo-applications, Chin. Chem. Lett. 31 (2020) 3055–3064.
[8] M. Wright, A. Uddin, Organic—inorganic hybrid solar cells: A comparative review, Sol. Energy Mater. Sol. Cells 107 (2012) 87–111.
[9] Q. Chen, H. Liu, H.-S. Kim, Y. Liu, M. Yang, N. Yue, G. Ren, K. Zhu, S. Liu, N.-G. Park, Y. Zhang, Multiple-stage structure transformation of organic-inorganic hybrid perovskite $CH_3NH_3PbI_3$, Phys. Rev. X 6 (2016) 031042.
[10] M. Grätzel, The light and shade of perovskite solar cells, Nat. Mater. 13 (2014) 838–842.
[11] P. Basumatary, P. Agarwal, A short review on progress in perovskite solar cells, Mater. Res. Bull. 149 (2022) 111700.
[12] M.K.A. Mohammed, G. Sarusi, P. Sakthivel, G. Ravi, U. Younis, Improved stability of ambient air-processed methylammonium lead iodide using carbon nanotubes for perovskite solar cells, Mater. Res. Bull. 137 (2021) 111182.
[13] X. Huang, J. Li, H. Fu, The first covalent organic-inorganic networks of hybrid chalcogenides: Structures that may lead to a new type of quantum wells, J. Am. Chem. Soc. 122 (2000) 8789–8790.
[14] X. Huang, J. Li, Y. Zhang, A. Mascarenhas, From 1D chain to 3D network: Tuning hybrid II-VI nanostructures and their optical properties, J. Am. Chem. Soc. 125 (2003) 7049–7055.
[15] Z.-X. Deng, L. Li, Y. Li, Novel inorganic-organic-layered structures: Crystallographic understanding of both phase and morphology formations of one-dimensional CdE (E=S, Se, Te) nanorods in ethylenediamine, Inorg. Chem. 42 (2003) 2331–2341.
[16] Y. Zhang, II-VI based organic-inorganic hybrid structures: Brief review and perspective, J. Lumin. 248 (2022) 118936.
[17] X. Huang, I.V. H.R. Heulings, V. Le, J. Li, Inorganic-organic hybrid composites containing MQ (II-VI) slabs: A new class of nanostructures with strong quantum confinement and periodic arrangement, Chem. Mater. 13 (2001) 3754–3759.
[18] T. Ye, M. Kocherga, Y.-Y. Sun, A. Nesmelov, F. Zhang, W. Oh, X.-Y. Huang, J. Li, D. Beasock, D.S. Jones, T.A. Schmedake, Y. Zhang, II–VI organic–inorganic hybrid nanostructures with greatly enhanced optoelectronic properties, perfectly ordered structures, and shelf stability of over 15 years, ACS Nano 15 (2021) 10565–10576.
[19] T. Ye, Y.-Y. Sun, M. Kocherga, A. Nesmelov, T.A. Schmedake, Y. Zhang, Degradation kinetics of organic–inorganic hybrid materials from micro-raman spectroscopy and density-functional theory: The case of β-ZnTe(en)$_{0.5}$, Small 19 (2023) 2302935.
[20] R. Mei, Y.-Z. Wang, X.-L. Liu, T.A. Schmedake, Y. Zhang, P.-H. Tan, Giant exciton binding energy in a three-dimensional organic–inorganic hybrid semiconductor, J. Am. Chem. Soc. jacs.5c15468.
[21] Y. Zhang, Z. Islam, Y. Ren, P.A. Parilla, S.P. Ahrenkiel, P.L. Lee, A. Mascarenhas, M.J. McNevin, I. Naumov, H.-X. Fu, X.-Y. Huang, J. Li, Zero thermal expansion in a nanostructured inorganic-organic hybrid crystal, Phys. Rev. Lett. 99 (2007) 215901.
[22] Y. Zhang, G.M. Dalpian, B. Fluegel, S.-H. Wei, A. Mascarenhas, X.-Y. Huang, J. Li, L.-W. Wang, Novel approach to tuning the physical properties of organic-inorganic hybrid semiconductors, Phys. Rev. Lett. 96 (2006) 026405.
[23] J.C. Miller, Y. Wang, Y. Zhang, T.A. Schmedake, M.D. McCluskey, Phase transitions of β-ZnTe(en)$_{0.5}$ under hydrostatic pressure, AIP Adv. 15 (2025) 045308.
[24] I.E. Collings, A.L. Goodwin, Metal–organic frameworks under pressure, J. Appl. Phys. 126 (2019) 181101.
[25] J. Wieme, S.M.J. Rogge, P.G. Yot, L. Vanduyfhuys, S.-K. Lee, J.-S. Chang, M. Waroquier, G. Maurin, V. Van Speybroeck, Pillared-layered metal–organic frameworks for mechanical energy storage applications, J. Mater. Chem. A 7 (2019) 22663–22674.
[26] Y. Wang, Y. Yang, X. Yang, B. Zou, Pressure effects on metal/covalent-organic frameworks: Structural and optical properties, Sci. China Chem. 67 (2024) 2890–2903.

[27] M. Erkartal, Giant negative linear compressibility, isosymmetric phase transition, and breathing effect in a 3D covalent organic framework, J. Phys. Chem. C 128 (2024) 588–596.
[28] X. Qian, X. Gu, R. Yang, Anisotropic thermal transport in organic–inorganic hybrid crystal β-ZnTe(en)$_{0.5}$, J. Phys. Chem. C 119 (2015) 28300–28308.
[29] A. Haxhijaj, S. Riemelmoser, A. Pasquarello, Lattice dynamics and structural phase stability of group-IV elemental solids with the r^{2}SCAN functional, Phys. Rev. B 113 (2026) 104105.
[30] G. Kresse, J. Furthmüller, Efficiency of ab-initio total energy calculations for metals and semiconductors using a plane-wave basis set, Comput. Mater. Sci. 6 (1996) 15–50.
[31] G. Kresse, D. Joubert, From ultrasoft pseudopotentials to the projector augmented-wave method, Phys. Rev. B 59 (1999) 1758–1775.
[32] P.E. Blöchl, Projector augmented-wave method, Phys. Rev. B 50 (1994) 17953–17979.
[33] J.P. Perdew, K. Burke, M. Ernzerhof, Generalized gradient approximation made simple, Phys. Rev. Lett. 77 (1996) 3865–3868.
[34] J.P. Perdew, A. Ruzsinszky, G.I. Csonka, O.A. Vydrov, G.E. Scuseria, L.A. Constantin, X. Zhou, K. Burke, Restoring the density-gradient expansion for exchange in solids and surfaces, Phys. Rev. Lett. 100 (2008) 136406.
[35] S. Grimme, J. Antony, S. Ehrlich, H. Krieg, A consistent and accurate *ab initio* parametrization of density functional dispersion correction (DFT-D) for the 94 elements H-Pu, J. Chem. Phys. 132 (2010) 154104.
[36] S. Grimme, S. Ehrlich, L. Goerigk, Effect of the damping function in dispersion corrected density functional theory, J. Comput. Chem. 32 (2011) 1456–1465.
[37] J. Sun, A. Ruzsinszky, J.P. Perdew, Strongly constrained and appropriately normed semilocal density functional, Phys. Rev. Lett. 115 (2015) 036402.
[38] J.W. Furness, A.D. Kaplan, J. Ning, J.P. Perdew, J. Sun, Accurate and numerically efficient r^{2}SCAN meta-generalized gradient approximation, J. Phys. Chem. Lett. 11 (2020) 8208–8215.
[39] H. Peng, Z.-H. Yang, J.P. Perdew, J. Sun, Versatile van der Waals density functional based on a meta-generalized gradient approximation, Phys. Rev. X 6 (2016) 041005.
[40] R. Sabatini, T. Gorni, S. De Gironcoli, Nonlocal van der Waals density functional made simple and efficient, Phys. Rev. B 87 (2013) 041108.
[41] M. Dion, H. Rydberg, E. Schröder, D.C. Langreth, B.I. Lundqvist, Van der Waals density functional for general geometries, Phys. Rev. Lett. 92 (2004) 246401.
[42] G. Román-Pérez, J.M. Soler, Efficient implementation of a van der Waals density functional: Application to double-wall carbon nanotubes, Phys. Rev. Lett. 103 (2009) 096102.
[43] J. Klimeš, D.R. Bowler, A. Michaelides, Van der Waals density functionals applied to solids, Phys. Rev. B 83 (2011) 195131.
[44] Y. Le Page, P. Saxe, Symmetry-general least-squares extraction of elastic data for strained materials from *ab initio* calculations of stress, Phys. Rev. B 65 (2002) 104104.
[45] G. Kresse, J. Furthmüller, J. Hafner, *ab initio* force constant approach to phonon dispersion relations of diamond and graphite, Europhys. Lett. 32 (1995) 729–734.
[46] K. Parlinski, Z.Q. Li, Y. Kawazoe, First-principles determination of the soft mode in cubic ZrO_2, Phys. Rev. Lett. 78 (1997) 4063–4066.
[47] A. Togo, I. Tanaka, First principles phonon calculations in materials science, Scr. Mater. 108 (2015) 1–5.
[48] A. Togo, First-principles phonon calculations with Phonopy and Phono3py, J. Phys. Soc. Japan 92 (2023) 012001.
[49] X. Gonze, C. Lee, Dynamical matrices, Born effective charges, dielectric permittivity tensors, and interatomic force constants from density-functional perturbation theory, Phys. Rev. B 55 (1997) 10355–10368.
[50] S. Baroni, S. De Gironcoli, A. Dal Corso, P. Giannozzi, Phonons and related crystal properties from density-functional perturbation theory, Rev. Modern Phys. 73 (2001) 515–562.
[51] M. Gajdoš, K. Hummer, G. Kresse, J. Furthmüller, F. Bechstedt, Linear optical properties in the projector-augmented wave methodology, Phys. Rev. B 73 (2006) 045112.
[52] D. Porezag, M.R. Pederson, Infrared intensities and Raman-scattering activities within density-functional theory, Phys. Rev. B 54 (1996) 7830–7836.
[53] R. Caracas, Raman spectra and lattice dynamics of cubic *gauche* nitrogen, J. Chem. Phys. 127 (2007) 144510.
[54] M. Bagheri, H.-P. Komsa, High-throughput computation of Raman spectra from first principles, Sci. Data 10 (2023) 80.
[55] J.M. Skelton, L.A. Burton, A.J. Jackson, F. Oba, S.C. Parker, A. Walsh, Lattice dynamics of the tin sulphides SnS_2, SnS and Sn_2S_3 : Vibrational spectra and thermal transport, Phys. Chem. Chem. Phys. 19 (2017) 12452–12465.
[56] D. Connétable, O. Thomas, First-principles study of the structural, electronic, vibrational, and elastic properties of orthorhombic NiSi, Phys. Rev. B 79 (2009) 094101.
[57] C.-Y. Moon, G.M. Dalpian, Y. Zhang, S.-H. Wei, X.-Y. Huang, J. Li, Study of phase selectivity of organic-inorganic hybrid semiconductors, Chem. Mater. 18 (2006) 2805–2809.
[58] A.M. Mazurek, M. Franczak-Rogowska, Ł. Szeleszczuk, Isosymmetric phase transitions in crystals: From subtle rearrangements to functional properties, Crystals 15 (2025) 807.
[59] A.R. Oganov, C.W. Glass, Crystal structure prediction using *ab initio* initio evolutionary techniques: Principles and applications, J. Chem. Phys. 124 (2006) 244704.
[60] Y. Wang, J. Lv, L. Zhu, Y. Ma, Crystal structure prediction via particle-swarm optimization, Phys. Rev. B 82 (2010) 094116.